Proceedings of the ASME 2020 39th International Conference on Ocean, Offshore and Arctic Engineering
OMAE2020
August 3-7, 2020, Virtual, Online

OMAE2020-18298

VALIDATION OF NUMERICAL WAVE TANK SIMULATIONS USING REEF3D WITH JONSWAP SPECTRA IN INTERMEDIATE WATER DEPTH

Csaba Pakozdi*
SINTEF Ocean, P.O.Box 4762 Sluppen
N-7465 Trondheim, Norway
Phone: +47 45 42 77 83
Email: csaba.pakozdi@sintef.no

Sebastien Fouques
Maxime Thys
SINTEF Ocean
N-7465 Trondheim, Norway

Arun Kamath
Weizhi Wang
Dept. of Civil and Env. Eng. NTNU
Trondheim, Norway

Fatemeh Hoseini Dadmarzi
Erin Bachynski
Dept. of Marine Tech. NTNU
Trondheim, Norway

Hans Bihs
Dept. of Civil and Env. Eng. NTNU
Trondheim, Norway

ABSTRACT

As offshore wind turbines increase in size and output, the support structures are also growing. More sophisticated assessment of the hydrodynamic loads is needed, particularly for the ultimate limit state design. For higher-order phenomena related to rare steep wave events such as ringing, a better understanding of the stochastic loads is needed. As an innovative step forward to reduce the cost of extensive model tests with irregular waves, a larger number of investigations can be carried out using high-performance high-fidelity numerical simulations after an initial stochastic validation with model test data.

In this paper, the open-source hydrodynamic model REEF3D::FNPF (Fully Nonlinear Potential Flow) is used to carry out three-hour long simulations with the JONSWAP spectrum in intermediate water depth conditions. Statistical properties of the free surface elevation in the numerical wave tank are validated using the available data from model tests carried out at SINTEF Ocean/NTNU. The spectral shape, significant wave height, peak period, skewness, kurtosis, and wave crest height statistics are compared. The results are analyzed and it is found that the numerical model provides reasonably good agreement with the model test data.

INTRODUCTION

In an earlier publication [1], measured regular waves were numerically reproduced by several numerical wave tanks. None of the tested numerical models gave acceptable free surface elevations when the measured free surface elevation or the measured wave maker motion was used for wave generation in the numerical model. Instead, analytical regular wave solutions were used to generate the waves numerically, by fitting the wave periods and the wave height to the experimentally recorded free surface elevation. There are several reasons for these discrepancies between numerical simulations and experimental results.

The mechanical generation of water waves in conventional experimental facilities can be hampered by the intrinsic boundary conditions of the laboratory. Wave reflection [2], spurious waves [3–5] and eigenmodes [6] are typical issues researchers must deal with when assessing model responses during test campaigns. However, in such facilities, the complex nonlinear physics of wave propagation is simply enforced by the laws of

*Address all correspondence to this author.

nature.

Numerical wave tanks (NWTs) face the opposite problem: boundary conditions can be flexible, but assumptions must be made, and shortcuts must be taken to be able to solve the propagation equations numerically in a reasonable amount of time. It is therefore important to check the quality of the waves generated by NWTs in terms of realistic physical properties.

In the present work, a new model test is chosen for validation. This model test was performed in June-July 2018 in the small wave tank at SINTEF Ocean [7, 8] as part of the research project WAS-XL [9]. The purpose of the test was documentation of wave kinematics and measurement of wave loads on rigid models. Compared to the SINTEF Ocean Basin, this facility is smaller and has a rigid flat bottom.

The REEF3D::CFD module has already been used as numerical wave tank (NWT) [10, 11]. The module solves the Navier-Stokes equations with a two-phase fluid model which makes the software able to simulate breaking waves [12–14].

The new numerical wave model FNPF of REEF3D solves the Laplace equation for the flow potential and the nonlinear kinematic and dynamics free surface boundary conditions [15]. Very promising results in the reproduction of experimental regular and bi-chromatics wave with constant water depth as well as with complex bottom topology have been presented with the open-source hydrodynamic model REEF3D::FNPF in [16] and [17]. This approach requires reduced computational resources compared to CFD based NWTs. The REEF3D::FNPF module can use the already implemented functionality of REEF3D [18], where solid boundaries are incorporated through a ghost cell immersed boundary method. Therefore it is capable of simulating wave-structure interaction such as complex sea bottom topography by solving the non-linear potential theory problem. The Laplace equation together with the enclosure of the boundary conditions are solved with a finite difference method on a stretched σ-coordinate system similar to OceanWave3D [19].

With a potential flow model, it is possible to simulate three-hours sea state without reducing the order of the waves which can be modeled and without the very long computational time of a two-phase Navier-Stokes solver [20, 21].

In this paper, the open-source hydrodynamic model REEF3D::FNPF is used to carry out three-hour long simulations with the JONSWAP spectrum in intermediate water depth conditions. Statistical properties of the free surface elevation in the numerical wave tank are validated using the available data from model tests carried out at SINTEF Ocean/NTNU. The spectral shape, significant wave height, peak period, skewness, kurtosis, and wave crest height statistics are compared. These comparison serves to check the quality of the waves generated by the NWT in term of realistic physical properties.

IMPLEMENTATION

The governing equation for the fully nonlinear potential flow model in REEF3D::FNPF is the Laplace equation:

$$\frac{\partial^2\Phi}{\partial x^2}+\frac{\partial^2\Phi}{\partial y^2}+\frac{\partial^2\Phi}{\partial z^2}=0. \tag{1}$$

Boundary conditions are required in order to solve for the velocity potential Φ from this elliptic equation, especially at the free surface and at the seabed. These are the kinematic and dynamic boundary conditions which must be fulfilled at all times and are prescribed as follows:

$$\frac{\partial\eta}{\partial t}=-\frac{\partial\eta}{\partial x}\frac{\partial\widetilde{\Phi}}{\partial x}-\frac{\partial\eta}{\partial y}\frac{\partial\widetilde{\Phi}}{\partial y}+\widetilde{w}\left(1+\left(\frac{\partial\eta}{\partial x}\right)^2+\left(\frac{\partial\eta}{\partial y}\right)^2\right) \tag{2}$$

$$\begin{aligned}\frac{\partial\widetilde{\Phi}}{\partial t}=-\frac{1}{2}\Bigg[&\left(\frac{\partial\widetilde{\Phi}}{\partial x}\right)^2+\left(\frac{\partial\widetilde{\Phi}}{\partial y}\right)^2\\&-\widetilde{w}^2\left(1+\left(\frac{\partial\eta}{\partial x}\right)^2+\left(\frac{\partial\eta}{\partial y}\right)^2\right)\Bigg]-g\eta\end{aligned} \tag{3}$$

where η is the free surface elevation, $\widetilde{\Phi}=\Phi(\mathbf{x},\eta,t)$ is the velocity potential at the free surface, $\mathbf{x}=(x,y)$ represents the location at the horizontal plane and $\widetilde{w}$ is the vertical velocity at the free surface.

The bottom boundary condition represents an impervious solid boundary:

$$\frac{\partial\Phi}{\partial z}+\frac{\partial h}{\partial x}\frac{\partial\Phi}{\partial x}+\frac{\partial h}{\partial y}\frac{\partial\Phi}{\partial y}=0,\ z=-h. \tag{4}$$

where $h=h(\mathbf{x})$ is the water depth measured from the still water level to the seabed.

The Laplace equation with the boundary conditions is solved with a finite difference method on a σ-coordinate system. A σ-coordinate system deforms with the free surface and is also flexible in the handling of irregular boundaries. The relationship between a Cartesian grid and a σ-coordinate is as follows:

$$\sigma=\frac{z+h(\mathbf{x})}{\eta(\mathbf{x},t)+h(\mathbf{x})}. \tag{5}$$

Several methods are implemented in REEF3D for grid stretching in horizontal and vertical direction. One of them uses the sinh

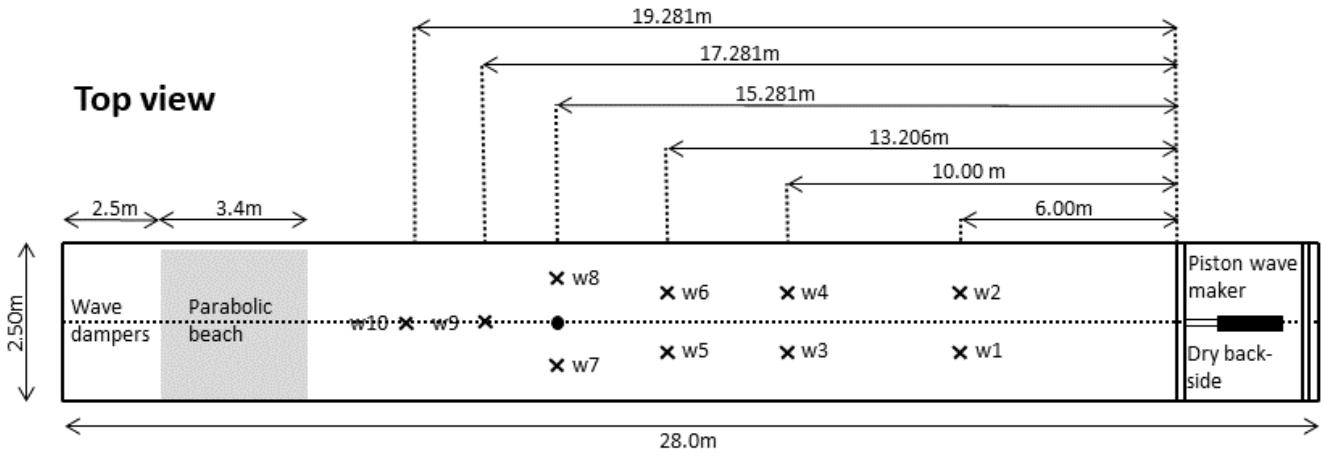

FIGURE 1: Small towing tank

function as the stretching function:

$$\tilde{\sigma} = 1 - \frac{\sinh(\delta(\sigma - 1))}{\sinh(-\delta)} \tag{6}$$

where σ is the uniform σ-coordinates, δ is the stretching factor and $\tilde{\sigma}$ is the new σ-coordinates. A larger value of δ defines a grid where the grid points are stretched close to the free surface and smaller value gives more uniform distribution of the vertical grid points. $\tilde{\sigma}$ will be referred as σ further in this paper. This stretching method is used in the simulations with uniform horizontal grid spacing. The grid is generated by REEF3D at the start of the simulation.

Once the velocity potential Φ is obtained in the σ-domain, the velocities can be calculated as follows:

$$u(\mathbf{x},z) = \frac{\partial \Phi(\mathbf{x},z)}{\partial x} = \frac{\partial \Phi(\mathbf{x},\sigma)}{\partial x} + \frac{\partial \sigma}{\partial x}\frac{\partial \Phi(\mathbf{x},\sigma)}{\partial \sigma}, \tag{7}$$

$$v(\mathbf{x},z) = \frac{\partial \Phi(\mathbf{x},z)}{\partial y} = \frac{\partial \Phi(\mathbf{x},\sigma)}{\partial y} + \frac{\partial \sigma}{\partial y}\frac{\partial \Phi(\mathbf{x},\sigma)}{\partial \sigma}, \tag{8}$$

$$w(\mathbf{x},z) = \frac{\partial \Phi(\mathbf{x},z)}{\partial z} = \frac{\partial \sigma}{\partial z}\frac{\partial \Phi(\mathbf{x},\sigma)}{\partial \sigma}. \tag{9}$$

The Laplace equation is discretized using a second-order central difference scheme and is solved using a parallelized geometric multigrid pre-conditioned conjugated gradient solver provided by Hypre [23].

The convection terms at the free-surface are discretized with the fifth-order Hamilton-Jacobi weighted essentially non-oscillatory (WENO) scheme [24]. A WENO discretization stencil is based on smoothness of three local ENO-stencils. The local stencil with the highest smoothness is assigned the highest weight and contributes the most significantly to the solution. The scheme is therefore capable of handling large gradients without instability.

For the time treatment, a third-order accurate TVD Runge-Kutta scheme [25] is used with a constant time step.

The model is fully parallelized following the domain decomposition strategy. Ghost cells are used to exchange information between adjacent domains and are updated with the values from the neighboring processors using the Message Passing Interface (MPI).

Wave generation in the numerical wave tank is handled using a Neumann boundary condition. Here, the spatial derivatives of the velocity potential are prescribed according to the wavemaker kinematics with help of ghost cells. This non+homogeneous Neumann boundary condition is defined by the difference scheme as follows:

$$\frac{\varphi_i - \varphi_{i-1}}{\triangle x} = u(x,z,t) \tag{10}$$

where $u(x,z,t)$ is the horizontal velocity of the wave maker, φ_{i-1} is the velocity potential at the ghost cells behind the inlet boundary, φ_i is the potential at the neighboring fluid cells, $\triangle x$ is the horizontal grid spacing and the index i defines the column number of the grid. The wave maker motion is defined through a time series of the piston locations. In this paper, the measured piston motion is used to generate the waves. An active absorption method is used to mitigate wave reflection presented in [22].

The breaking model presented in [20] is used in the simulation with a reduced viscosity damping value. The influence of the parameters used in this breaking model on the waves is studied in [26].

TABLE 1: Main parameters of the sea state

H_s [m]	T_p [s]	γ
8.0	10.0	5.0

EXPERIMENTAL DATA

The model tests for the documentation of wave kinematics and for the measurement of wave loads on rigid models were carried out at Froude scale of 1:50 [7, 8]. The tank is equipped with a wave maker and a towing carriage. Two types of wave makers are available: a single flap hinged wave maker and a piston type wave maker. In this study, the piston type wave maker was used based on considerations related to efficiency and parasitic waves. At the other end of the tank is a beach, with an adjustable height depending on the water depth. The main dimensions of the towing tank are: length 28 m, breadth 2.5 m, water depth between 0 and 1.0 m (model scale). The coordinate system is a right handed coordinate system, centred on the seabed at the mean position of the wave maker at the bottom of the tank. The positive x-axis points in the direction of wave propagation and the positive z-axis points upwards. The model setup is shown in Figure 1.

For the wave kinematics, the wave elevation was measured at 11 different locations for different regular and irregular waves, with two water depths of 27m and 33m. The 11th locations is not

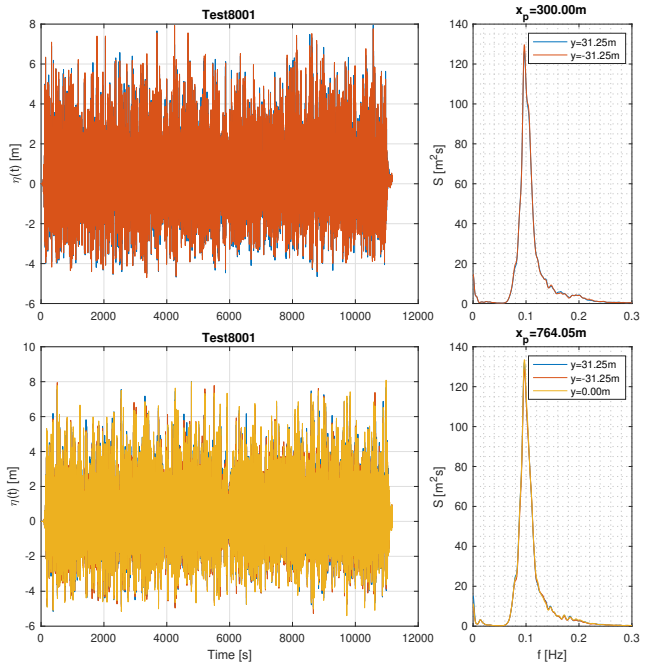

FIGURE 2: Measured time series of the first three-hours realization of the sea state at different locations and their power spectra

TABLE 2: Main wave components

	Shortest wave	Peak period wave	Longest wave
T [s]	0.675	1.42	4.00
f [Hz]	1.482	0.70	0.25
L [m]	0.71	2.68	9.00
C_{ph} [m/s]	1.05	1.89	2.25

labeled in Figure 1 only its location is shown. This is the location of the mono-pile model. Wave elevation was measured using resistive wave probes. The tank is shown with the wave probes in Figure 1. The wave, flap position, temperature, and load signals were sampled at 200Hz (model scale) with Butterworth filter at 20Hz (model scale).

This paper focuses on the the validation of one of the irregular sea states for 27m water depth. The main parameters of the sea state is presented in Table 1. This sea state was realized with 20 seed variations. Three hour realizations were used, based on the JONSWAP wave spectrum. The significant wave height H_s and peak wave period T_p were chosen from the 50 year contour line for a selected location from the MARINA Platform FP7 project [27] (site 15, North Sea Centre).

As shown in Figure 1, the wave height is measured at several locations at the same distance from the wave maker. In this way, the homogeneity of the wave field in the tank can be evaluated. The degree of difference in the homogeneity at different locations can be observed as shown in Figure 2. The comparison of the power spectrum indicates a transverse oscillation in the tank but is not significant. The location of the wave probes does not aid in the estimation of the wave reflection from the beach but it is estimated to be about 10% based on the observations from the regular wave tests.

VALIDATION

The simulations are set up in model scale but the result are presented in full scale.

SETUP As previously shown [28], the vertical grid stretching has significant effect on the wave dispersion property in the numerical simulation. A method of identifying the optimum stretching for a given wave period, which yields the correct wave propagation velocity, is also presented by Pakozdi et al. [28]. This method can be extended for irregular wave simulations. Three periods are identified defining the grid size and the time step:

- the shortest wave with the lowest phase velocity

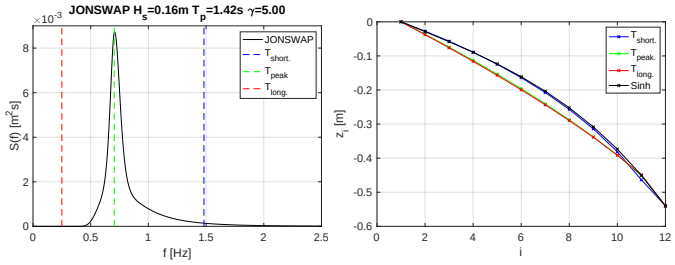

(a) JONSWAP spectrum (b) Vertical grid locations

FIGURE 3: Representation of the main parameter for the numerical setup and the vertical grid spacing (model scale)

- the peak period wave with highest energy in the power spectrum
- the longest wave with the largest phase velocity

The length of the shortest wave defines the horizontal grid size: $dx = \lambda/35 = 0.02$ m. The phase velocity of the longest wave defines the time step: $dt = dx/C_{ph} = 0.0089$ s, based on the values presented in Table 2. The location of these periods related to the wave power spectrum is shown in Figure 3a. The wave period of the shortest wave corresponds to the limit of the wave maker. During the investigation six difference sea states with several seed numbers are simulated. The same shortest and longest wave periods are used to define the grid for all sea states. The period of longest wave is defined at the period where the energy of the JONSWAP spectrum is about 1% of the maximum energy level. However, the longest wave period is not defined from the spectrum which is presented in this paper.

The vertical grid spacing is chosen to be close to the optimal distribution of all three waves. The optimal vertical grid distribution for all three wave periods, labeled as 'Tshort', 'Tpeak' and 'Tlong' as well as the applied vertical distribution, labeled as 'Sinh' is presented in Figure 3b. As mentioned earlier the sinh function is used to stretch the grid points vertically. The distribution and the number of the vertical grid points of the applied vertical grid points are close to the optimal grid stretching of the shortest wave. The dimension of the numerical wave tank is given in Figure 4. The numerical wave tank is used in the simulations has the same depth as the physical tank. The length of the NWT is larger than the physical tank. Different lengths of numerical beach were tested before choosing the active wave absorption method. In order to test the long numerical beach, the length of the NWT was significantly increased relative to the physical tank. After applying the active absorption outlet condition the length of the NWT is not changed because the best results are observed with this configuration.

COMPARISON OF ONE REALIZATION As mentioned earlier, the measured piston motions are used in the simulations. This gives the possibility to make a deterministic, direct comparison between the model test and the numerical simulation. In this section the first seed number numerical realization is matched with its model test.

During the parameter study[1] of different numerical setups it was observed that the active absorption method to mitigate wave reflection, which is described by [10], gives significantly better agreement between measured time series than a relaxation zone based wave damping. Two reasons were found which might explain the better agreement between the measurement and the numerical simulation with the active absorption outlet condition.

The comparison of the time history of the mean water levels shown in Figure 5 demonstrate that a low frequency motion of the free surface is triggered during the simulation which only the active wave absorption is able to damp. The exciting modes do not correspond any eigenmodes of the tank ($L = 56$ m). The lower diagram of this figure shows the estimated volume flux at the inlet due to the piston motion. The magnitude of the volume change is significantly lower than the change of the mean water level. One can conclude that the mean water level changes less with active absorption than with the relaxation zone. This might be the reason for the better agreement between model test and numerical results.

The second reason for the better agreement is the similar wave reflection behavior between the model test and the numerical simulation with active absorption. Because the location of the free surface elevation is known for each time step at all locations, it is possible to split the free surface elevation into incoming and reflected wave by use of two-dimensional Fourier-transformation from space-time representation to wave number and wave frequency representation [29]. Estimation of the reflected wave time series at wave gauge location 4 shows (Figure 6) that the significant wave height of the reflected wave time series is about 11% of the incident wave time series, i.e. 11% of the waves are reflected by the outlet in the numerical simulation. A direct comparison of the measured time series and the simulation is presented for a short time window in Figure 7. One can observe a very good agreement regarding the phase between the time series. There are two more trends which are observed in this diagram, which is also present in all the numerical simulations:

[1] Due to the lack of space only the final numerical results are presented.

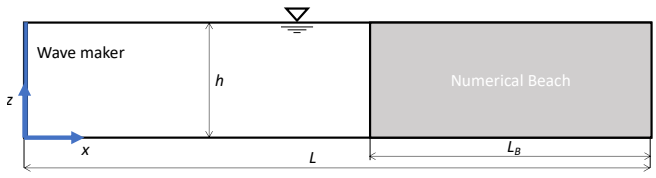

FIGURE 4: Numerical wave tank with numerical beach wave absorption $L = 56.0$m, $L_B = 5.9$m, $h = 0.54$m (model scale)

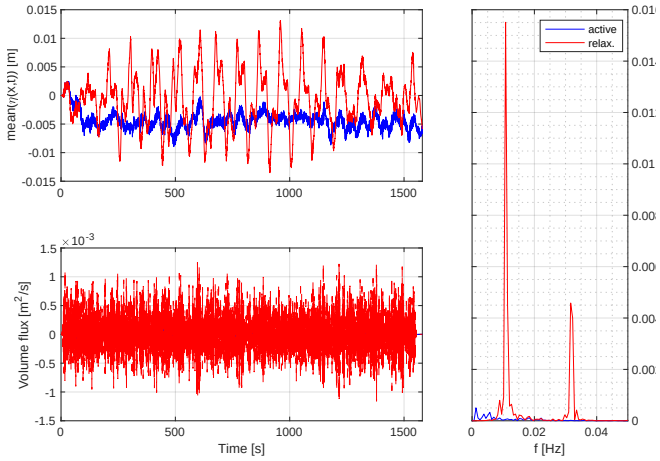

FIGURE 5: The mean position of the free surface elevation and the volume flux at the inlet boundary in the numerical model with different methods to mitigate wave reflection

- The crest height of the larger, steeper waves are taller in the simulations but it is the opposite for the smaller waves
- The wave trough for most of the smaller waves is deeper in the simulation but it is the opposite for the larger, steeper waves.

This indicates that the set-down effect is larger in the numerical simulation.

The most interesting location for further investigation is the position of the mono-pile, which is placed at $x_p = 764.05$ m from the wave maker. The comparison of the spectrum of the measured and simulated three hours time series shows fair agreement

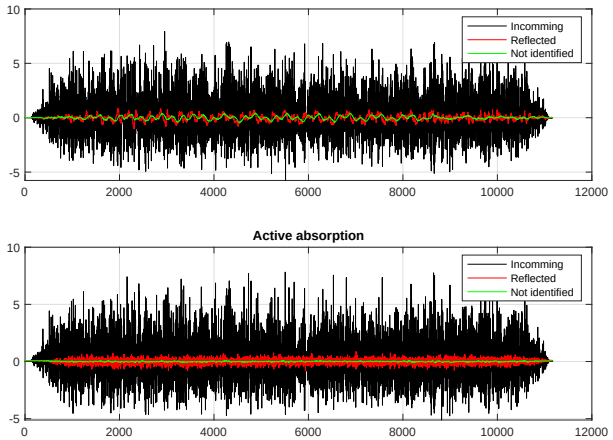

FIGURE 6: The free surface elevation at $x_p = 764.05$ m in the numerical model, split into incoming and reflected waves

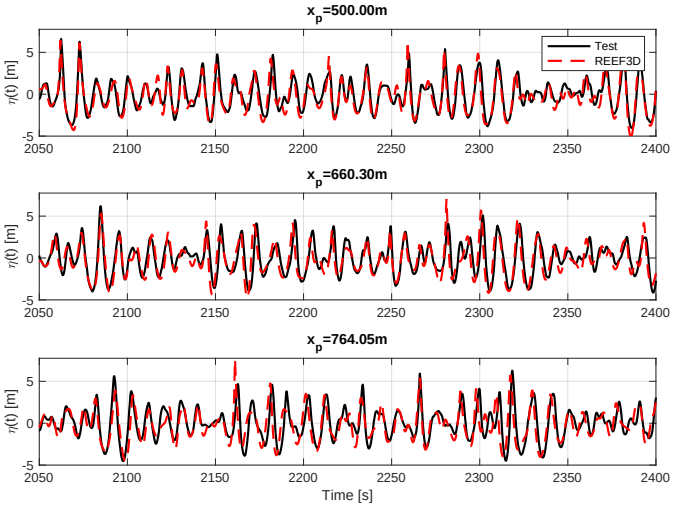

FIGURE 7: Comparison of the free surface elevation at $x = 764.05$ m

between the spectrum in Figure 8. A very good agreement is seen both in the low frequency range and the high frequency range. This indicates that the applied numerical setup is able to resolve the small waves and correctly simulates the nonlinear wave-wave interaction, not only in the low frequency but also in the high frequency range. Around the peak period the waves have less energy in the numerical simulation. The shoulders of the measured spectrum at $f = 0.08$Hz and at $f = 1.05$Hz are missing or not so strongly shaped in the numerical simulation. However the significant wave height of the numerical spectrum is slightly larger ($H_s = 7.725$ m versus $H_s = 7.60$ m) but the peak periods are the same $T_p = 10.41$s.

The result of the zero-up crossing analysis is presented as the Weibull plot of the cumulative probabilities of the whole three hours time series in Figure 9. The above mentioned trends re-

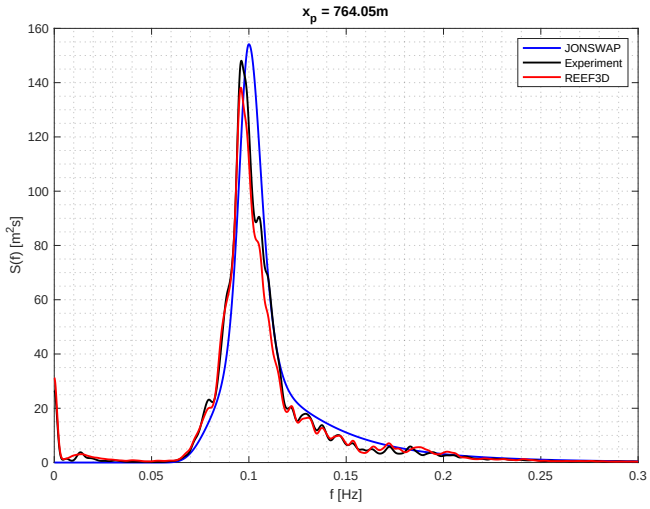

FIGURE 8: Power Spectrum of the free surface elevation at $x = 764.05$m (location of the mono-pile)

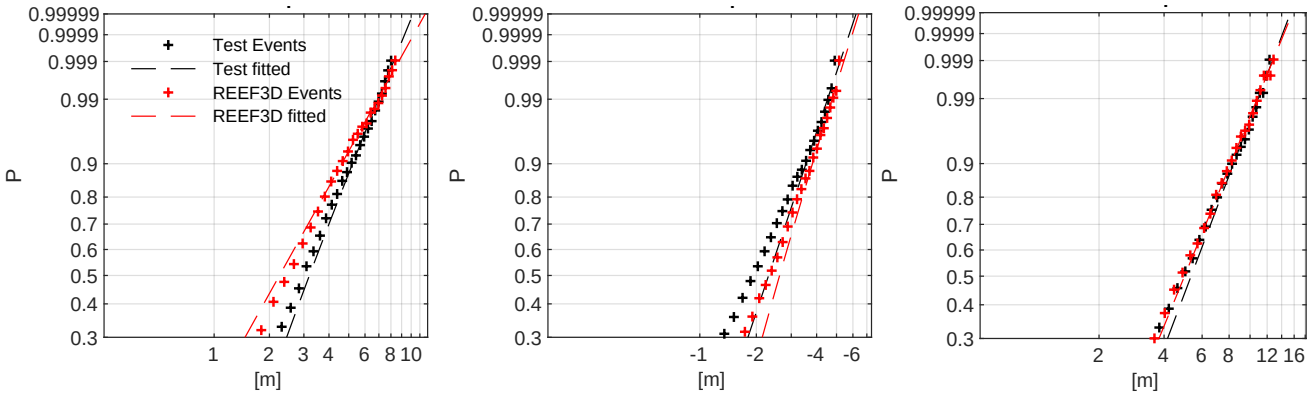

(a) Wave crest (b) Wave trough (c) Wave height

FIGURE 9: Weibull plot of cumulative probability of the wave crest, trough and height at $x_p = 764.05$m (location of the mono-pile)

garding the set-down can be clearly observed in the Weibull plot of the cumulative probabilities of the three hours time series in Figure 9. Waves are smaller in the simulations than in experiment if the crest heights are less than 6 m, but if the crest heights are larger than 6 m the numerical waves are larger. (Figure 9a). The opposite can be see with the trough statistics in Figure 9c. The effect of the combination of these two trends is a very good agreement between the measurement and the numerical simulation regarding to the wave heights. The larger crest height at the steep large wave in the simulation can be explained by the wave breaking model in the REEF3D::FNPF not damping the waves which might break in the experiment. Therefore, the skewness of the numerical time series is slightly larger than the measured one, 0.365 versus 0.332. The good agreement between the measured and simulated steep and large waves, the very good phase between the time series, and less good agreement between smaller waves can be observed in the other 19 realizations (not shown here).

COMPARISON OF TWENTY REALIZATIONS In the stochastic validation of the numerical simulation, the records of twenty experimental realizations of the same sea state will be used for comparison with twenty numerical realizations where the experimental piston motions are used to generate the waves for each corresponding sea state. As exemplified by the first seed in the previous paragraphs, the deterministic comparison shows a good agreement between model test data and numeric.

The significant wave height represents the potential energy of the free surface elevation. The local variations of the significant wave height average as well as the extreme values and standard deviation is shown as error bar diagram in Figure 10.

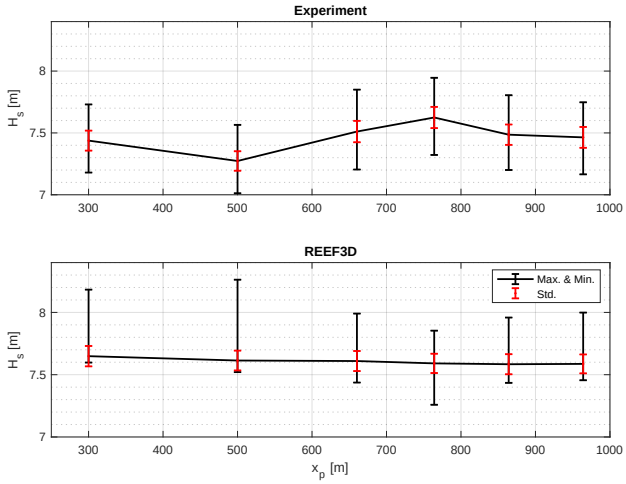

FIGURE 10: Comparison of the significant wave height at all locations

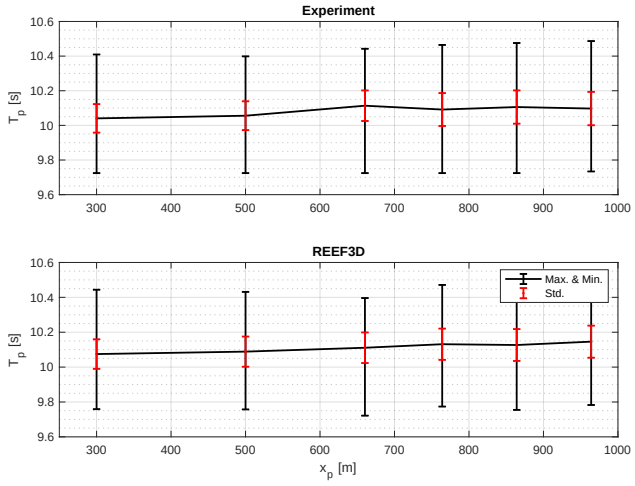

FIGURE 11: Comparison of the peak period at all locations

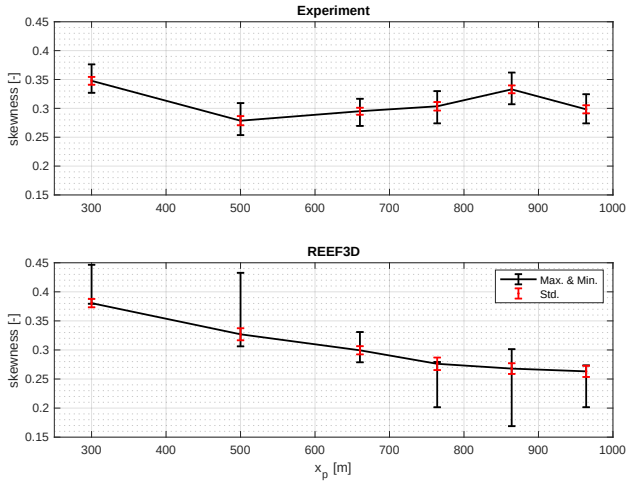

FIGURE 12: Comparison of the skewness at all locations

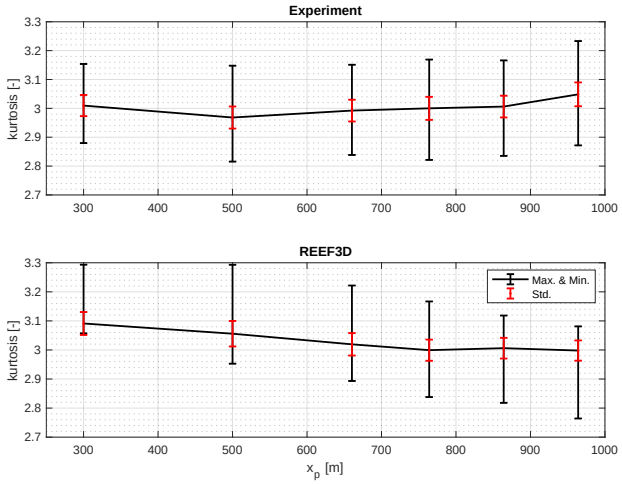

FIGURE 13: Comparison of the kurtosis at all locations

The black line represents the mean value of H_s, the end points of black beams show the highest and the lowest value and the size of the red beams represents the standard deviations. The largest mean value is recorded at $x_p = 764.05$ m in the experiment, which indicates the location of the highest waves. However, the mean value of H_s almost does not change in the numerical simulation, which suggests a constant energy level of the waves along the numerical domain. The variation of the H_s values is the about the same (similar standard deviation of H_s). The extreme values are symmetrically located around the mean values in the experimental records. The numerical simulations shows an asymmetry in the location of the extreme values with regard to the position of the mean values, the largest value is further from the mean value than the lowest value.

The peak period of a spectrum shows the wave period in which the most energy is concentrated. Comparison of the peak periods shows (Figure 11) the same trend in the model test and in the numerical records, with a slight increase of the mean value at longer distances from the wave maker. The standard deviation of the T_p as well as the extreme values symmetry are similar.

The skewness and kurtosis parameters characterizes the nonlinearity of the surface elevation.

The skewness of the time series measures the symmetry of a signal, zeros value means that the crest height and the trough have the same size, positive values indicate a larger crest than trough. The numerical simulations show the largest skewness in the mean value closest to the wave maker (Figure 12). This is about 0.38 which corresponds to the value estimated from a second-order approximation from [30]:

$$\begin{aligned} \text{skewness} &= \frac{34.4 H_s}{g T_p^2} + 2.14 \times 10^{-4} \left(\frac{g T_p^2}{h} \right)^3 \\ &= \frac{34.47.54}{g 10.1^2} + 2.14 \times 10^{-6} \left(\frac{g 10.1^2}{27.0} \right)^3 \\ &= 0.37 . \end{aligned} \tag{11}$$

The skewness becomes lesser at larger distances from the wave maker and stabilizes around a value of 0.27 at the last three locations. The skewness of the measured time series varies without any spatial pattern. Its largest value equals 0.33 at $x_p = 864.05$m. The variation of the skewness values at the same location is slightly less in the experiment than in the numerically estimated time series. The extreme values are located symmetrically around the mean value in the experimental data. This symmetry is not observed in the numerical records, there is much larger deviation of the extreme values from the mean value.

The kurtosis diagram show the same spatial trends as observed for the skewness in Figure 13. The largest value of the mean value of the kurtosis estimated from the numerical simulations can be observed closest to the wave maker. It is slightly lower with a value of 3.1 compared to the value of 3.14 approximated using the following formula ([30]):

$$\text{kurtosis} = 3 + 3 \times \text{skewness}^2 = 3 + 3 \times 0.37^2 = 3.14 . \tag{12}$$

One can observe a stabilization of the kurtosis value around 3.0 at the last three locations. The averaged kurtosis values of the experiments are slightly lower than the numerical simulation

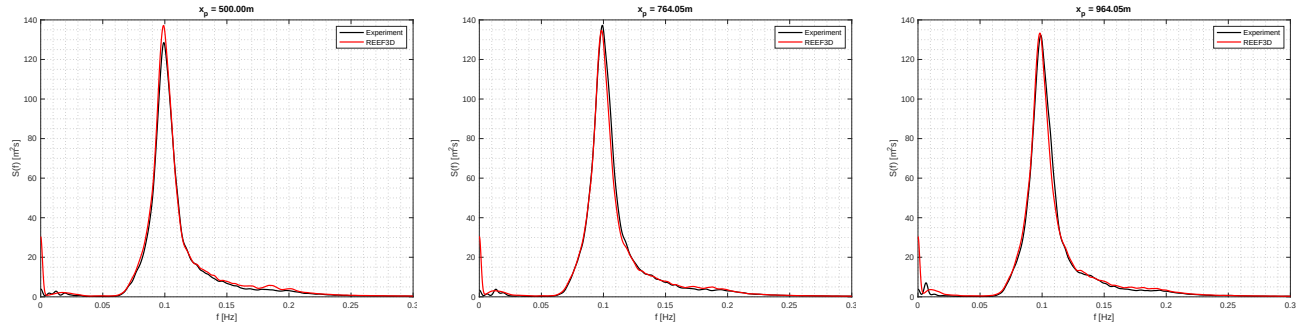

(a) $x_p = 500.00$m (b) $x_p = 764.05$m (c) $x_p = 964.05$m

FIGURE 14: Comparison of the averaged spectrum at three locations

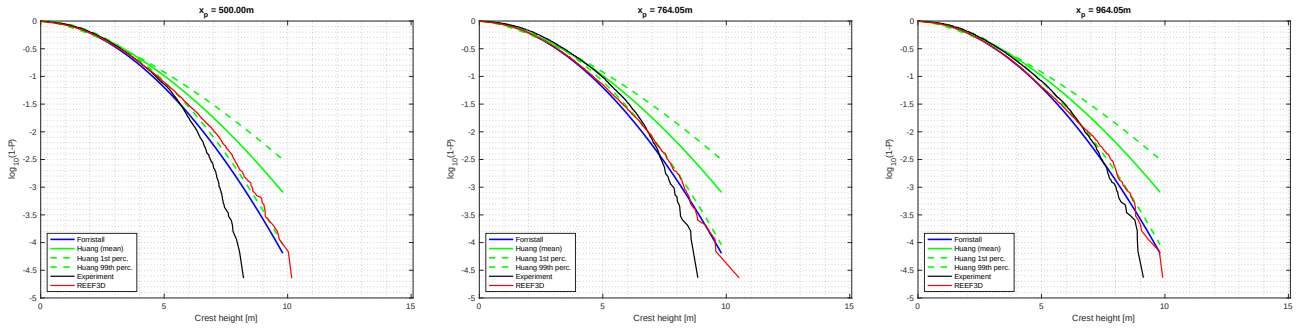

(a) $x_p = 500.00$m (b) $x_p = 764.05$m (c) $x_p = 964.05$m

FIGURE 15: Distributions of the crest height, ensemble of all wave events

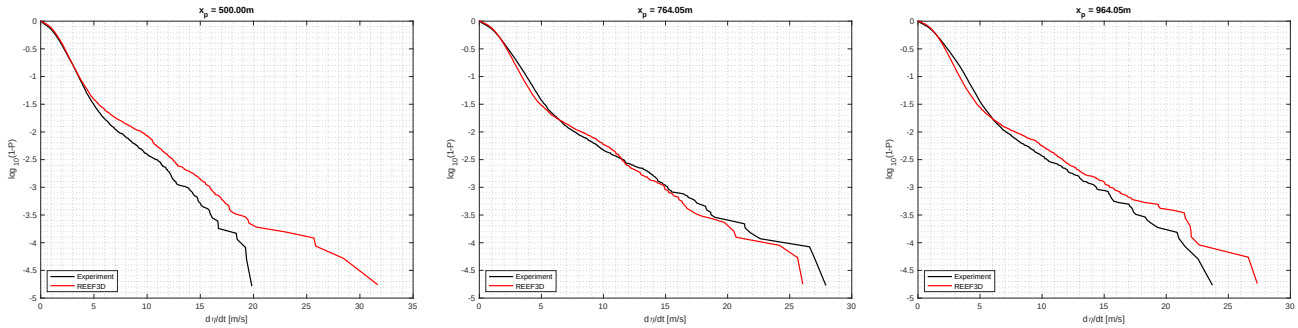

(a) $x_p = 500.00$m (b) $x_p = 764.05$m (c) $x_p = 964.05$m

FIGURE 16: Distribution of the maximum elevation rise velocity $\partial\eta/\partial t$, ensemble of all wave events

around 3.0 and also varies less spatially. The extreme values are located symmetrically around the mean value here as well, which is not the case with the numerical simulations.

The similar values of the significant wave height and peak period are not sufficient criteria to judge the similarity between two time series. The shape of the spectrum is also an important criteria for the validation. The average of the twenty spectra are compared in Figure 14 at three different locations. Because of the smoothing effect of the averaging, the shape of these spectra are very smooth and they are very similar to each other. The largest differences are at the peak period at all three locations similar to the trend observed in the deterministic validation.

The wave crest heights and the free surface rise velocity $\partial\eta/\partial t$ are used to characterize the kinematics at the free surface. The wave slope $\partial\eta/\partial x$ can be checked through the elevation rise velocity $\partial\eta/\partial t$ at a point in space since the nonlinear kinematic free surface conditions in (2) contains the wave slope.

The ensemble distribution of the crest heights is usually

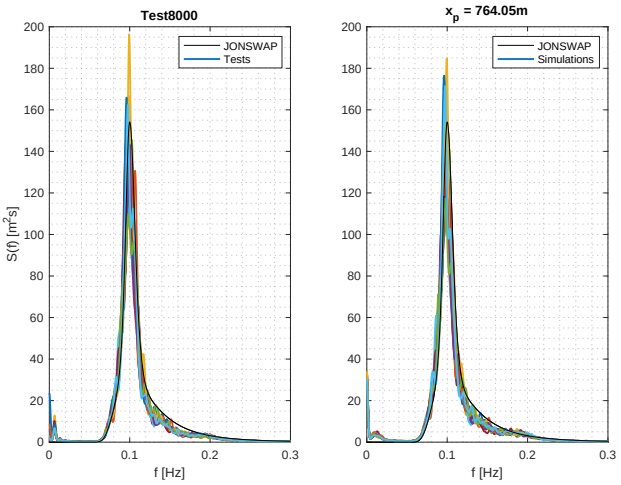

FIGURE 17: Comparison of all spectrum at $x_p = 764.05$m (location of the mono-pile)

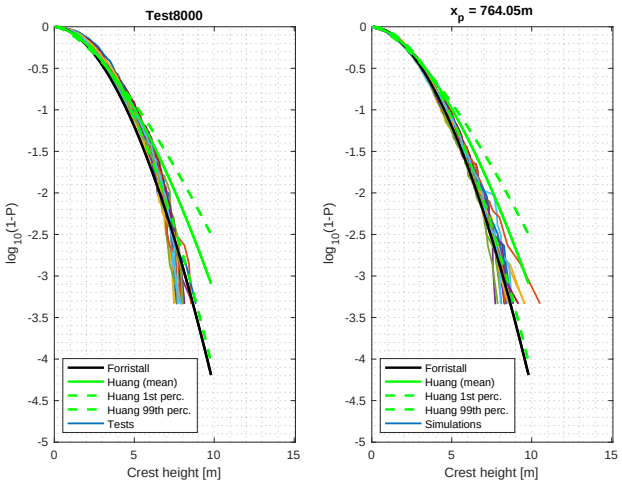

FIGURE 18: Comparison of all three-hours ensembles of the crest heights at $x_p = 764.05$ (location of the mono-pile)

compared with the second-order Forristall distribution which is presented as a blue line in the diagrams of Figure 15. Huang & Zhang [31] give a formula defining the mean, the upper 99th and lower 99th percentiles of the wave crest heights. These formulae are based on a regression analysis of nonlinear numerical simulations with the JONSWAP spectrum with peak enchantment parameters γ between 1 and 4. These values are presented in green in the diagrams. The investigated sea state has a $\gamma = 5.0$ which explains the higher crest height values of the curves. The crest height distribution of the measured wave events of all twenty realizations is coincident with the Forristall distribution or slightly over this curve for waves with up to 6-7 m crest height at all distances from the wave maker. Over this value, the distribution of the measured crest heights lie under the line, which can indicate wave breaking in the experiments and the dissipation of energy due to breaking. The same trend can be observed here which is already mentioned in the comparison of one realization. The waves with crest heights higher than 6 m are overestimated in the numerical model, which closely follows the Forristall distribution. This can yield a more conservative estimation of the extreme values than the experimental data predicts. Due to the smaller waves being underestimated by the simulations, the numerical simulations can predict lower hydrodynamic loads for fatigue analysis than the experimental data.

When all wave events of the twenty realizations are included in the ensemble, the most probable value for a three-hours realization for an exceedence of 10^{-3} is obtained. This value is overestimated by the numerical simulations at all locations. However this overshoot decreases with increasing distance from the wave maker.

The free surface rise velocity $\partial\eta/\partial t$ is calculated by second order central finite differential scheme without any additional filtering. This can yield higher extreme values but the choice of filtering parameters can also have a significant influence on the high values. The comparison of all events in Figure 16 shows that the steepness of the largest numerical waves at locations Figure 16a and 16c is remarkably larger than the measured waves rise velocity over a value of 6 m/s. The most probable value for a three-hours realization for an exceedence of 10^{-3} is also larger. Both distributions, from the experiments and from the numerical simulations are very much similar in Figure 16a. The numerical simulations slightly under predict the wave steepness except the steepest wave, where a significant difference can be observed at the tail. Here, at this location the most probable value for a three-hours realization is almost the same for the experimental and the numerical results.

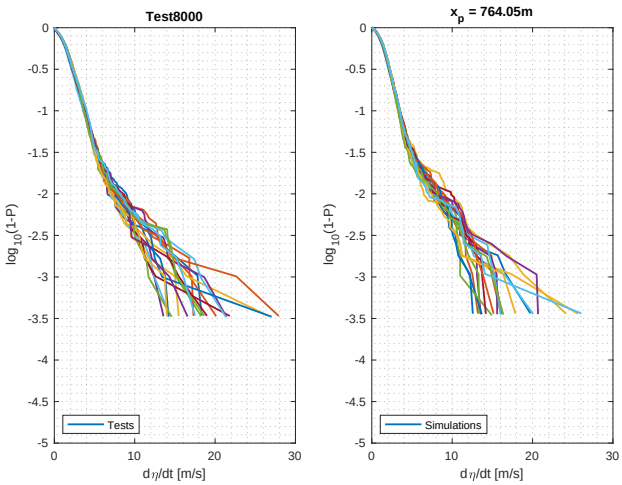

FIGURE 19: Comparison of all three-hours ensembles of the maximum elevation rise velocity $\partial\eta/\partial t$ at $x_p = 764.05$m (location of the mono-pile)

The above presented results give a global overview of all twenty realizations. The presentation of the three-hours simulation in addition to the other diagrams can give a better insight into the statistical differences between the individual realization. As in the deterministic validation, only the results at the location of the mono-pile $x_p = 764.05$ m are presented in this paper.

Overlaying the spectra shows that the variation of the spectrum shape is similar for the experiment and the numerical simulations but not entirely identical in Figure 17. The largest differences are seen mostly around the peak period. The highest peak of the experimental spectrum is not captured by the numerical simulation (yellow lines).

The overlaid diagram of the wave crest height distributions shows that except for one numerical realization (red line) with overestimated extreme values in Figure 18, the distributions are similar.

The overlaid diagrams of the maximum free surface rise velocity indicates a similar trend in Figure 19, the distribution of the three-hours extreme is similar to each other except for one experimental realization with a very high value (red line) in the experiment.

CONCLUSION

In this paper, the open-source hydrodynamic model REEF3D::FNPF is used to carry out three-hour long simulations with the JONSWAP spectrum in intermediate water depth conditions. Statistical properties of the free surface elevation in the numerical wave tank at several locations are validated using available data from model tests carried out at SINTEF Ocean/NTNU. The spectral shape, significant wave height, peak period, skewness, kurtosis, wave crest height as well as the maximum free surface rise velocity statistics are compared. The results are analyzed and it is found that the numerical model provides reasonably good agreement with the model test data. Based on the result of the statistical comparison we can conclude that the waves generated by NWT have realistic physical properties.

Using a coupling to simulate the largest wave events using two-phase CFD simulations can yield a better agreement between the experiment and numerical simulations as the breaking wave can be more appropriately handled. This is planned for the next phase of the project. After the validation of the free surface properties, the further step is to use the wave kinematics proposed by the numerical simulations to define the hydrodynamic load for structural analysis similar to that presented by Pakozdi et al. [1]. The stochastic comparison of the resulting structure response against the measured response forces can give the final answer about the physical realism of the numerical simulation.

ACKNOWLEDGMENT

The authors are grateful to the grants provided by the Research Council of Norway under WAS-XL project (No. 268182).

REFERENCES

[1] Pakozdi, C., Spence, S., Fouques, S., Thys, M., Alsos, H. S., Bachynski, E. E., Bihs, H., and Kamath, A., 2018. "Nonlinear wave load models for extra large monopiles". In Proceedings of ASME 2018 1st International Offshore Wind Technical Conference, no. IOWTC2018-1083.

[2] Zelt, J. A., and Skjelbreia, J., 1992. "Estimating incident and reflected wave fields using an arbitrary number of gauges". In Coastal Engineering, pp. 777–789.

[3] Stansberg, C. T., 2006. "Laboratory modelling for floating structures in shallow water". In Proceedings of the 25th International Conference on Ocean, Offshore and Artic Engineering. OMAE2006-92496.

[4] Naciri, M., Bunnik, T., Buchner, B., and Huijsmans, R. H. M., 2004. "Low frequency motions of LNG carriers moored in shallow water". In Proceedings of the 23th International Conference on Ocean, Offshore and Artic Engineering. OMAE2004-51169.

[5] Schaffer, H. A., 1996. "Second-order wave maker theory for irregular waves". *J. of Ocean Engineering*, pp. 47–88.

[6] van Essen, S., Pauw, W., and van der Berg, J., 2016. "How to deal with basin modes when generating irregular waves on shallow water". In Proceedings of the 35th International Conference on Ocean, Offshore and Artic Engineering. OMAE2016-54134.

[7] Thys, M., 2019. Model test report: Wave kinematics and loads. Tech. Rep. OC2019 F-079, SINTEF Ocean.

[8] H. Dadmarzi, F., Thys, M., and Bachynski, E. E., 2019. "Validation of Hydrodynamic Loads on a Large-Diameter Monopile in Regular Waves". In International Conference on Offshore Mechanics and Arctic Engineering, Vol. Volume 7A: Ocean Engineering. V07AT06A060.

[9] WAS-XL Home page. https://www.sintef.no/projectweb/was-xl/.

[10] Miquel, A. M., Kamath, A., Alagan Chella, M., Archetti, R., and Bihs, H., 2018. "Analysis of different methods for wave generation and absorption in a CFD-based numerical wave tank". *Journal of Marine Science and Engineering,* ***6***(2).

[11] Bihs, H., Kamath, A., Chella, M. A., Aggarwal, A., and Øivind A. Arntsen, 2016. "A new level set numerical wave tank with improved density interpolation for complex wave hydrodynamics". *Computers & Fluids,* ***140***, pp. 191 – 208.

[12] Ahmad, N., Bihs, H., Myrhaug, D., Kamath, A., and Øivind A. Arntsen, 2019. "Numerical modeling of breaking wave induced seawall scour". *Coastal Engineering,* ***150***, pp. 108 – 120.

[13] Chella, M. A., Bihs, H., and Myrhaug, D., 2019. "Wave impact pressure and kinematics due to breaking wave impingement on a monopile". *Journal of Fluids and Structures,* ***86***, pp. 94 – 123.

[14] Bihs, H., Kamath, A., Alagan Chella, M., and Arntsen, O. A., 2009. "Extreme wave generation, breaking, and impact simulations using wave packets in REEF3D". *J. Offshore Mech. Arct. Eng.,* ***141***(4).

[15] Wang, W., Kamath, A., Pakozdi, C., and Bihs, H., 2019. "Investigation of focusing wave properties in a nume- rical wave tank with a fully nonlinear potential flow model". *Journal of Marine Science and Engineering, Journal of Marine Science and Engineering,* ***7***(375). Issue 10.

[16] Bihs, H., Wang, W., Pakozdi, C., and Kamath, A., 2020. "A flexible fully nonlinear potential flow solver". *Journal of Offshore Mechanics and Arctic Engineering,* ***accepted***.

[17] Pakozdi, C., Wang, W., and Bihs, H., 2019. "Validation of a high-performance computing nonlinear potential theory based numerical wave tank for wave structure interaction". In Coastal Structures 2019, T. S. Nils Goseberg, ed., Bundesanstalt fur Wasserbau.

[18] Moideen, R., Ranjan Behera, M., Kamath, A., and Bihs, H., 2019. "Effect of girder spacing and depth on the solitary wave impact on coastal bridge deck for different airgaps". *Journal of Marine Science and Engineering*.

[19] Bingham, H. B., and Zhang, H., 2007. "On the accuracy of finite-difference solutions for nonlinear water waves". *J Eng Math,* ***58***, pp. 211–228.

[20] Baquet, A., Kim, J., and Huang, Z., 2017. "Numerical modeling using cfd and potential wave theory for three-hour nonlinear irregular wave simulations". In ASME 2017 36th OMAE, no. OMAE2017-61090.

[21] Huang, Z., and Guo, Q., 2017. "Semi-empirical crest distribution of long-crested nonlinear waves of three-hour duration". In Proceedings of the 36th International Conference on Ocean, Offshore and Artic Engineering. OMAE2017-61226.

[22] Miquel, A., Kamath, A., Alagan Chella, M., Archetti, R., and Bihs, H., 2018. "Analysis of different methods for wave generation and absorption in a cfd-based numerical wave tank". *Journal of Marine Science and Engineering,* ***6***(2), p. 73.

[23] Falgout, R. D., Jones, J. E., and Yang, U. M., 2006. "Conceptual interfaces in hypre". *Future Gener. Comput. Syst.,* ***22***(1-2), Jan., pp. 239–251.

[24] Guang-Shan, J., and Chi-Wang, S., 1996. "Efficient implementation of weighted eno schemes". *Journal of Computational Physics,* ***126***(1), pp. 202–228.

[25] Chi-Wang, S., and Stanley, O., 1988. "Efficient implementation of essentially non-oscillatory shock-capturing schemes". *Journal of Computational Physics,* ***77***(2), August, pp. 439–471.

[26] Pakozdi, C., Kamath, A., Wang, W., and Bihs, H., 2020. "Representation of breaking wave kinematics in the fully nonlinear potential flow model reef3d::fnpf". In Proceedings of ASME 2020 39th International Conference on Ocean, Offshore and Arctic Engineering. OMAE2020-18160.

[27] Li, L., Gao, Z., and Moan, T., 2013. "Joint environmental data at five european offshore sites for design of combined wind and wave energy concepts". In Proceedings of the 32th International Conference on Ocean, Offshore and Artic Engineering.

[28] Pakozdi, C., Wang, W., Kamath, A., and Bihs, H., 2019. "Definition of the vertical spacing of a sigma grid based on the constant truncation error". In 10. National Conference on Computational Mechanics, B. Skallerud and H. I. Andersson, eds.

[29] Fonseca, N., Tahchiev, G., Stansberg, C. T., Fouques, S., and Rodrigues, M., 2020. "Model tests and numerical prediction of the low frequency motions of a fpso in shallow water with a wave splitting method". In 39th International Conference on Ocean, Offshore and Arctic Engineering. OMAE2020-18806.

[30] Vinje, T., and Haver, S., 1994. "On the non-Gaussian structure of ocean waves". In Seventh International Conference on the Behaviour of Offshore Structures (BOSS).

[31] Huang, J., and Zhang, Y., 2018. "Semi-empirical single realization and ensemble crest distributions of long crest nonlinear waves". In Proceedings of the 37th International Conference on Ocean, Offshore and Artic Engineering. OMAE2018-78192.